

# Performance of Silicon Drift Detectors at LCLS

G. Blaj\*, *Member, IEEE*, C. J. Kenney, *Member, IEEE*, S. Boutet, G. Carini, *Member, IEEE*, M. Chollet, G. Dakovski, G. Haller, *Member, IEEE*, P. Hart, S. Herrmann, J. Koglin, M. Messerschmidt, S. Nelson, J. Pines, S. Song, J. Thayer, A. Tomada, *Member, IEEE*, G. Williams

**Abstract**—Silicon drift detectors (SDDs) are a well-established technology that has revolutionized spectroscopy in fields as diverse as geology and dentistry. At a first glance it would seem that detectors with such a slow response would not be suitable for the new ultra-fast x-ray free-electron lasers (FEL) coming online.

However, for a subset of experiments at FELs, SDDs can make substantial contributions. Many measurements involve only several distinct photon energies known a priori, allowing pile-up deconvolution and accurate spectroscopic photon counting. Often the unknown spectrum is interesting, carrying science data, or the background measurement is useful to identify unexpected signals.

We investigated the performance of SDDs at x-ray FELs, in particular the ability to deconvolve the spectrum that results from various combinations of a few wavelengths and the possibility of separately recording photons that are absorbed at different radii (thus having varying drift times).

The analytic approach presented here permits isolating individual photon energies and interaction radii from pile-up events of 0 to 5 photons sampled from 6 monochromatic lines in a single SDD with accurate pile-up deconvolution, timing extraction and clipping correction.

The usefulness of SDDs will continue into the x-ray FEL era of science. Their successors, the ePixS hybrid pixel detectors, already offer hundreds of pixels with similar performance in a compact, robust and affordable package.

**Keywords**—*Silicon Drift Detectors, Free-Electron Lasers, Spectroscopy, Photon Counting, Spectroscopic Imaging*

## I. INTRODUCTION

Silicon drift detectors (SDDs) [1] are a well-established technology that has revolutionized spectroscopy in fields as diverse as geology and dentistry. At a first glance it would seem that detectors with such a slow response would not be suitable for the new ultra-fast x-ray free-electron lasers (FEL) coming online [2].

However, FELs require a range of detectors with different requirements to cover the applications space [3]. For a subset of experiments at FELs, SDDs can make substantial contributions.

---

Manuscript received November 30, 2016. SLAC-PUB-16878.

G. Blaj, C. J. Kenney, S. Boutet, G. Carini, M. Chollet, G. Dakovski, G. Haller, P. Hart, S. Herrmann, J. Koglin, M. Messerschmidt, S. Nelson, J. Pines, S. Song, J. Thayer, A. Tomada and G. Williams are with SLAC National Accelerator Laboratory, Menlo Park, CA 94025, U.S.A.

M. Messerschmidt is currently with State University of New York, Buffalo, NY 14203, U.S.A. and G. Williams is currently with Brookhaven National Laboratory, Upton, NY 11973, U.S.A.

\* Corresponding author: blaj@slac.stanford.edu

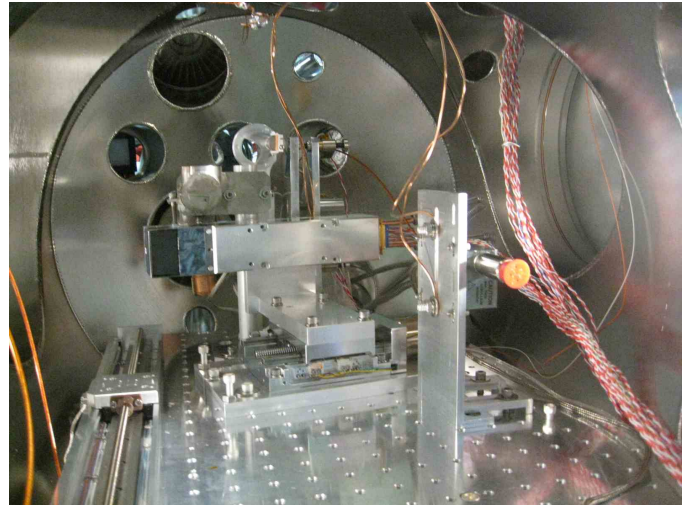


Fig. 1. Coherent X-ray Imaging instrument at LCLS: sample chamber with CSPAD 140K detector and silicon drift detector (SDD) installed. The SDD has a red plastic cap over its entrance window to protect its beryllium window.

Many measurements involve only several distinct photon energies known a priori, allowing pile-up deconvolution [4] and accurate spectroscopic photon counting. Often the unknown spectrum is interesting, carrying science data, or the background measurement is useful to identify unexpected signals.

We investigated the performance of silicon drift detectors at x-ray FELs. In particular we studied the ability to deconvolve the spectrum that results from various combinations of a few wavelengths and the possibility of separately recording photons that are absorbed at different radii (thus having varying drift times).

## II. METHODS

### A. Experimental Set-up

The experiments were performed at the Linac Coherent Light Source (LCLS) at SLAC National Accelerator Laboratory. Two LCLS instruments were used, X-ray Pump-Probe (XPP) [5] and Coherent X-ray Imaging (CXI) [6]. Fig. 1 shows the CXI experimental chamber, with a CSPAD [7] and SDD detector visible.

We projected FEL beam pulses of  $\sim 9$  keV photons on an Fe target (at FELs, the photon energy and beam intensity are somewhat variable from pulse to pulse), resulting in a detected signal composed of scattered 9 keV radiation together with Fe fluorescence (Fe  $K\alpha$  at 6.40 keV and Fe  $K\beta$  at 7.06 keV).

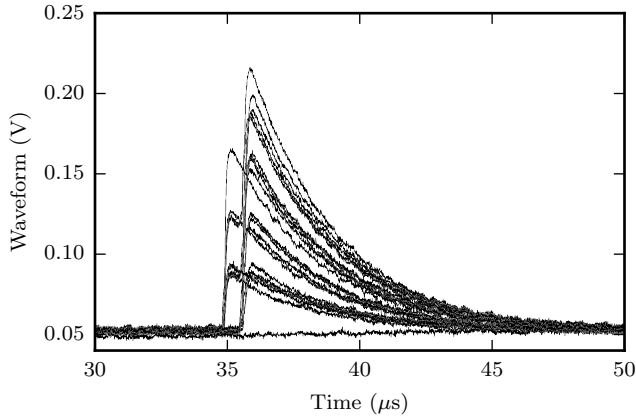


Fig. 2. Example of 20 randomly selected waveforms, showing pile-up of 0 to 3 photons peaks (central aperture) and 0 to 4 photons (peripheral aperture) on the y axis, and two clearly separated detection times on the x axis (around 35  $\mu$ s), corresponding to the 2 different apertures.

We acquired 354 304 pulses and corresponding waveforms at 120 Hz.

We used a standard Amptek XR-100SDD detector with a collimator with two cylindrical apertures ( $\sim 500 \mu$ m diameter), placed over the SDD such that one aperture was aligned with the center of the SDD and the other was at a  $\sim 2.5$ mm radius towards the periphery of the SDD. We will subsequently refer them as the "central" and "peripheral" apertures.

The SDD current was amplified and high-pass filtered with an Amptek PX5 Digital Pulse Processor and its analog differentiator output (see [8] for details) was routed to an Acquiris high-speed digitizer which was acquiring waveforms of 8192 samples at 100 MHz for each FEL pulse and was triggered pulse by pulse by the low jitter LCLS trigger signal.

### B. Analysis

Typically the pulse height analysis can be optimally performed in the frequency domain [9]. Here we chose to perform the analysis in the time domain, yielding accurate pileup, timing and clipping reconstruction.

Fig. 2 shows an example of 20 randomly selected scope traces, with peaks of 0 to 3 photons (central aperture) and 0 to 4 photons (peripheral aperture) and two corresponding, clearly separated timings on either side of  $t=35 \mu$ s.

Preliminary checks showed significant noise components at 40 MHz and 80 MHz components, which were removed with corresponding notch filters in the frequency domain. Other noise sources probably include the imperfect matching of the pulse processor analog output with the digitizer input and range and likely affect the reconstructed energy resolution.

Each individual waveform was then fitted (least squares) with a function:

$$y(t) = \min\left(y_0 + \frac{A_c \cdot e^{-\frac{t-t_c}{\tau_d}}}{1 + e^{-\frac{t-t_c}{\tau_{sc}}}} + \frac{A_p \cdot e^{-\frac{t-t_p}{\tau_d}}}{1 + e^{-\frac{t-t_p}{\tau_{sp}}}}, y_{max}\right), \quad (1)$$

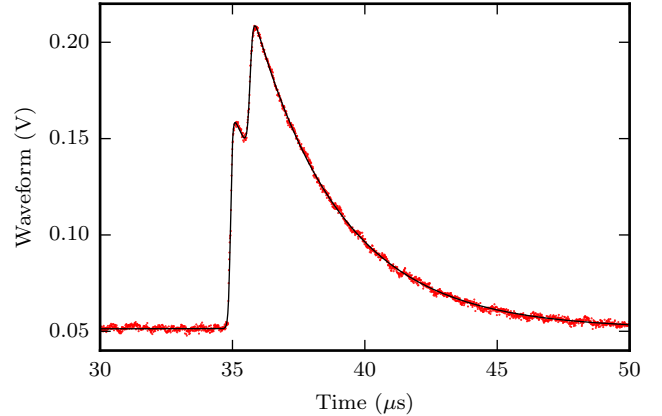


Fig. 3. For each event (i.e., FEL pulse and trigger), fitting (least squares, Eq. 1) central and peripheral aperture traces with their respective amplitudes ( $A_c$  and  $A_p$ ), timing ( $t_c$  and  $t_p$ ) information, despite pile-up or occasional clipping. This particular trace shows an example with 3 photons entering through the central aperture and 1 photon through the peripheral aperture.

where the signals induced by photons entering through the central and peripheral apertures have amplitudes  $A_c$  and  $A_p$ , arrival times  $t_c$  and  $t_p$ , with 'decay' and 'step' times denoted by  $\tau_d$ ,  $\tau_{sc}$  and  $\tau_{sp}$ , offset  $y_0$  and maximum (clipping) digitized voltages  $y_{max}$ .

Fig. 3 shows an example of waveform (red dots) and corresponding least squares fit (black line), with 3 photons entering through the central aperture and 1 photon entering through the peripheral aperture.

## III. RESULTS

### A. Pulse Arrival Times and Interaction Radii

Arrival time results are shown in Fig. 4(a); the pulse arrival times for the central aperture (black line,  $t_c = 34.928 \pm 0.011 \mu$ s) and peripheral (red line,  $t_p = 35.665 \pm 0.037 \mu$ s) are clearly separated.

The difference of 737 ns in pulse arrival times is due to the charge diffusion time between the SDD periphery and center. The arrival time jitter (11 ns in the center and 37 ns in the periphery) is significantly lower than the difference of arrival times, allowing precise pulse by pulse measurement of arrival times (and corresponding interaction radii), effectively turning the SDD into a position sensitive detector with tens of independent position channels and increasing resolution towards the center.

### B. Decay and Step Characteristic Times

Time results from fitting Eq. 1 are summarized in Fig. 4 with (a) histograms of arrival times (central and peripheral), (b) decay characteristic time (common) and (c) step characteristic times (central and peripheral).

The decay time shown in Fig. 4(b) has a relatively small variation ( $\sigma/\text{mean} \sim 3.2\%$ ). The step characteristic times depicted in Fig. 4(c) are clearly different, with a faster step

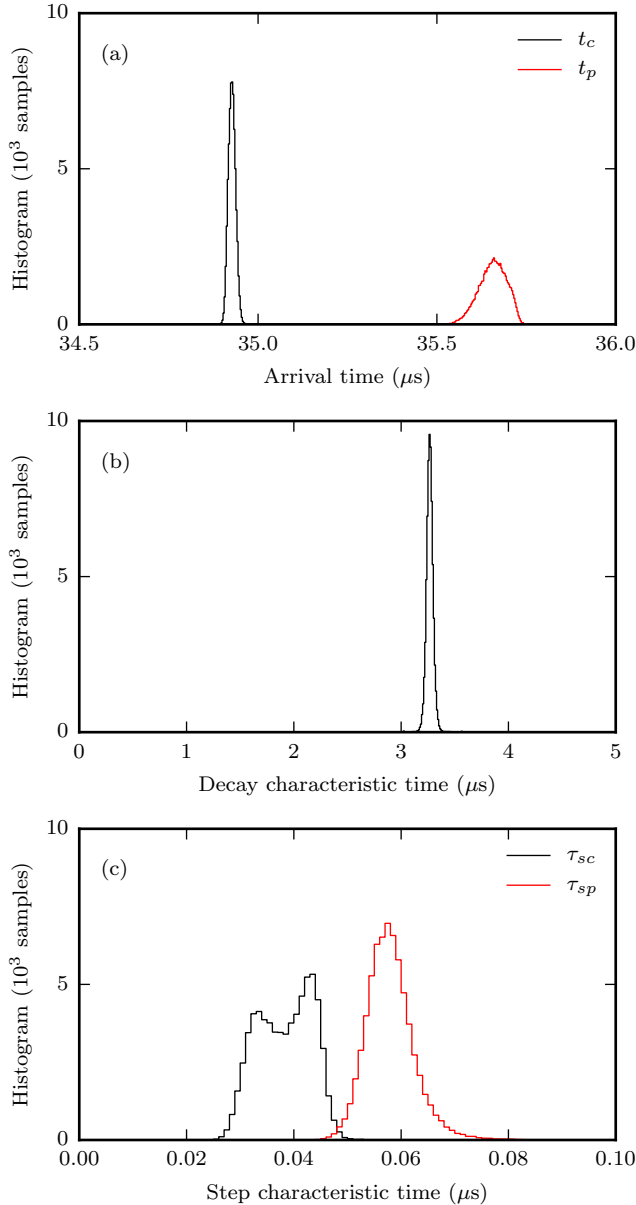


Fig. 4. Distribution of fitting results: (a) shows a histogram of pulse arrival times  $t_c = 34.928 \pm 0.011 \mu\text{s}$  (black line, central aperture) and  $t_p = 35.665 \pm 0.037 \mu\text{s}$  (red line, peripheral aperture). The difference of 737 ns is due to the difference of charge diffusion times and effectively turns the SDD into a position sensitive detector with tens of independent channels and increasing resolution towards the SDD center; (b) shows the histogram of the decay characteristic time  $\tau_d = 3.293 \pm 0.107 \mu\text{s}$ , and (c) shows the histogram of step characteristic times  $\tau_{sc} = 155 \pm 21 \text{ ns}$  (black line, central aperture) and  $\tau_{sp} = 234 \pm 21 \text{ ns}$  (red line, peripheral aperture).

transition in the central compared to the peripheral area; as both signals are processed identically, the difference is due to the supplementary charge dispersion between the periphery and center.

### C. Virtual Multichannel Spectra from Single SDD

Pulse amplitude results from fitting measurements with Eq. 1 are shown in Fig. 5 with a bi-dimensional histogram of the two amplitudes ( $A_p$  along the x axis,  $A_c$  along the y axis, logarithmic z axis). Multiple clusters of different combinations of energies can be observed.

Fig. 5 inset shows the area corresponding to 1 photon entering through each of the two apertures (in total, 2 photons). Three lines can be identified along each axis, with energies Fe K $\alpha$  (6.40 keV), Fe K $\beta$  (7.06 keV), and the nominal (9 keV) FEL line. Pile-up of 2 photons sampled from 3 lines each yields  $3^2 = 9$  ellipsoids.

The pattern corresponding to Fig. 5 inset repeats, with increasing complexity and (for this photon rate) decreasing intensity, for higher numbers of photons along each of the axes in Fig. 5. However, the pile-up results in clearly separable ellipsoids from each combination of: number of photons of each individual energy entering through each of the 2 apertures. The pile-up can be unambiguously reconstructed while retaining the multichannel information.

The ellipsoids are more elongated along an axis at  $\frac{3\pi}{4}$  (rotated counterclockwise from the x axis), meaning that the sum of the two amplitudes is typically more accurate than the difference. This is to be expected, as the sum of the amplitudes for signals entering through both apertures can be evaluated using many more samples compared to the difference of the amplitudes (limited to the relatively small set of samples between  $t_c$  and  $t_s$ , see for example Fig. 3).

### D. Response Linearity

In Fig. 6, circles correspond to the centroids of selected ellipsoids from Fig. 5. Both dimensions are stacked on the same plot. The colors, black and red, represent the central and peripheral apertures, respectively. The criteria for selecting ellipsoids was to represent energies resulting only from pile-up of known energies (i.e., Fe K $\alpha$  and Fe K $\beta$ ) and containing at least 100 photons each. This resulted in up to 3 photons for the central aperture and up to 4 photons through the peripheral aperture.

Lines represent corresponding linear fits, with the resulting relationships between energy and pulse amplitudes:  $A_c = -1.05 \times 10^{-4} \text{ V} + E_c \cdot 5.942 \times 10^{-3} \text{ V keV}^{-1}$  and  $A_p = -0.005 \times 10^{-4} \text{ V} + E_p \cdot 6.028 \times 10^{-3} \text{ V keV}^{-1}$ . The central gain is slightly smaller than the peripheral gain (with a ratio of 98.6%). Both fits show good response linearity.

### E. Single Photon Spectrum

In Fig. 7 we show a spectrum of (mostly) single photons entering through either aperture (red dots), up to 10 keV. The plot is shown on a square root scale to allow visualisation of both intense and weak lines. Along the 3 expected lines, there are a few other lines present; using the energy-amplitude relationships in subsection III-D, we identified the six fundamental lines as: Al K $\alpha$ , Ti K $\alpha$ , Cr K $\alpha$ , Fe K $\alpha$ , Fe K $\beta$ , and the nominal 9 keV line from the FEL beam, and labeled the peaks accordingly.

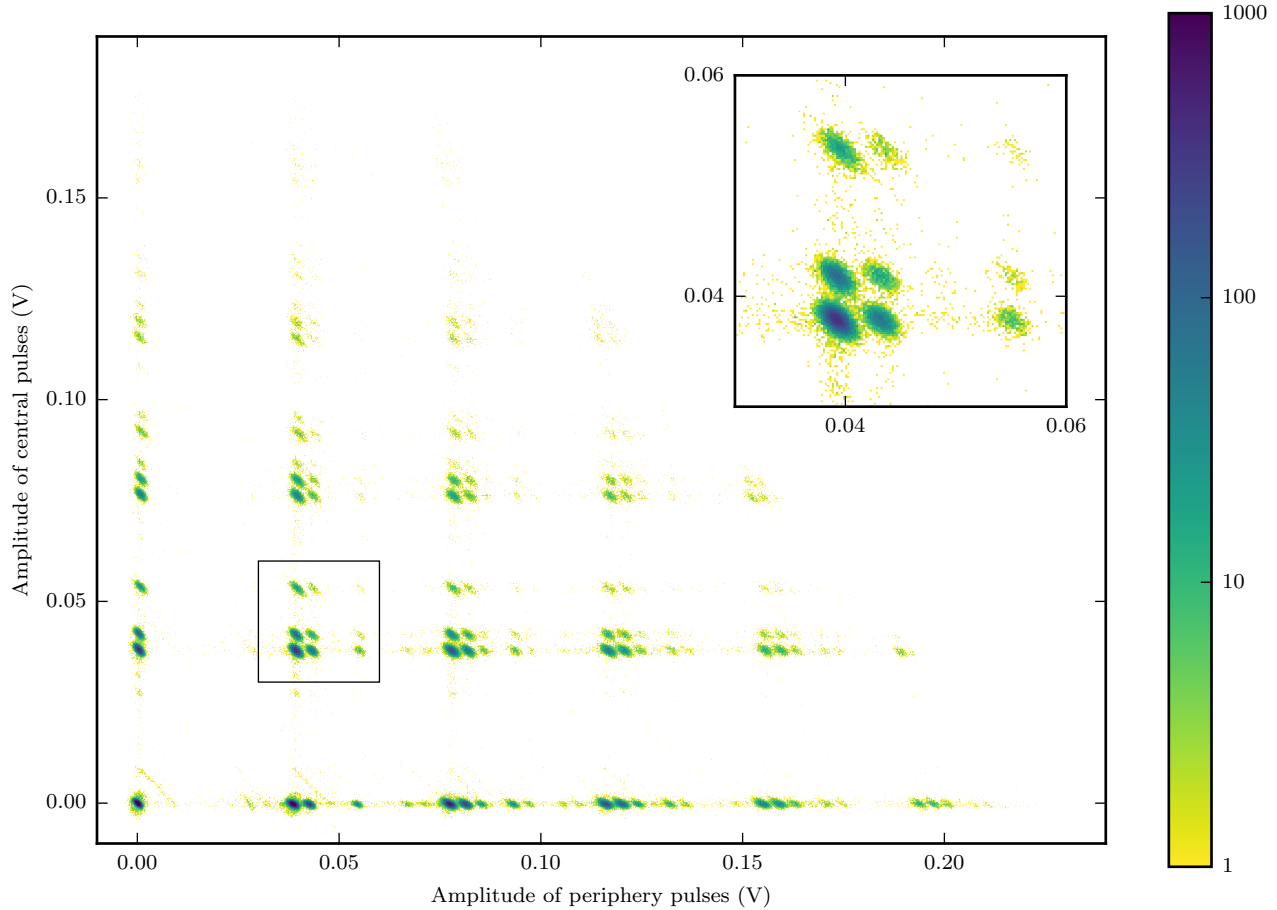


Fig. 5. Each waveform fit yields two amplitudes,  $A_c$  and  $A_p$ , corresponding to photons entering the SDD through the central and peripheral apertures. Here we show an image (on logarithmic scale) of the bidimensional histogram of these values,  $A_c$  along y axis,  $A_p$  along x axis). Different numbers of photons (0 to 5 photons along x, 0 to 3 photons along y) with different energies (sampled from Fe  $K\alpha$  at 6.40 keV, Fe  $K\beta$  at 7.06 keV, and FEL beam at  $\sim 9$  keV) enter through the two apertures yielding a complex histogram. However, the pile-up results in clearly separable ellipsoids from which the number of photons of each individual energy entering through each of the two apertures can be unambiguously reconstructed. The ellipsoids are more elongated along an axis at  $\frac{3\pi}{4}$ , meaning that the sum of the two amplitudes is typically more accurate than the difference. The inset shows a close-up of the area corresponding to one photon entering through each of the two apertures at the 3 different energies, yielding 9 ellipsoids.

The black line depicts the least squares fit using 7 Gaussian peaks (6 fundamental lines plus 1 zero peak) and a second degree polynomial background (dotted line). This allows us to measure the relative intensities (areas of 6 peaks), and also to conclude that the nominal 9 keV beam is actually closer to 9.1 keV.

The small peak at  $\sim 8$  keV does not represent a new fundamental line, but the pile-up of the Al  $K\alpha$  and Fe  $K\alpha$  1 photon peaks. While also  $K\beta$  peaks of Al, Ti and Cr must be present, their yield is much lower than the corresponding  $K\alpha$  yield; together with the low  $K\alpha$  intensity, their contribution can be neglected.

#### F. Spectral Pile-up Deconvolution

Fig. 8 depicts the entire spectrum of photons entering through either aperture (red dots), up to 37 keV; to facilitate

inspection of both intense and weak lines, the plot uses a square root y axis. The 6 fundamental lines (single photons) are clearly visible. Multiple photons pile-up (up to 5 shown) results in increasing complexity of the detected spectrum and decreasing intensity (in this particular case).

The black line depicts the least squares fit using a fitting model with theoretical peak positions of the 7 fundamental lines (zero peak, Al  $K\alpha$ , Ti  $K\alpha$ , Cr  $K\alpha$ , Fe  $K\alpha$ , Fe  $K\beta$ , and  $\sim 9$  keV) and their relative intensities (as determined in subsection III-F and Fig. 7), accurate models for pile-up and peak width as functions of energy, a second-degree polynomial for the background (dotted line), and a Poisson process model.

Fitting is remarkably successful in matching the characteristics of the plethora of peaks, using only the attributes of the fundamental peaks (determined in subsection III-E) and mathematical modeling. The average photon rate corresponding to this spectrum is  $1.768 \text{ photons } s^{-1}$ . In fact the FEL beam does

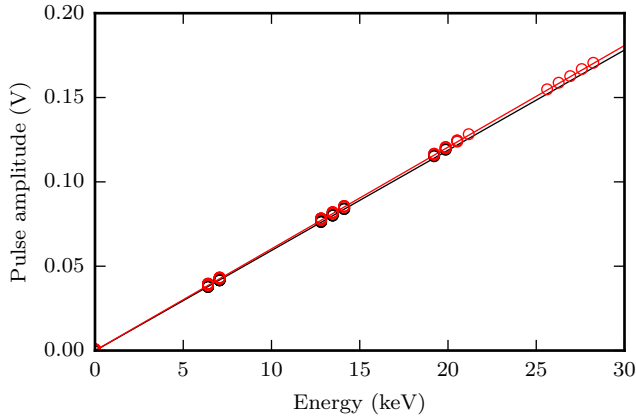


Fig. 6. Circles correspond to the centroids of selected ellipsoids in Fig. 5 (selected for precisely known energies as combinations of Fe  $K\alpha$  and Fe  $K\beta$  and containing at least 100 photons each). The colors, black and red, represent the central and peripheral apertures, respectively. Lines represent corresponding linear fits, with the resulting relationships between energy and pulse amplitudes:  $A_c = -1.05 \times 10^{-4} \text{ V} + E_c \cdot 5.942 \times 10^{-3} \text{ V keV}^{-1}$  and  $A_p = -0.005 \times 10^{-4} \text{ V} + E_p \cdot 6.028 \times 10^{-3} \text{ V keV}^{-1}$ . The central gain is slightly smaller than the peripheral gain, with a ratio of 98.6%. Both fits show good response linearity.

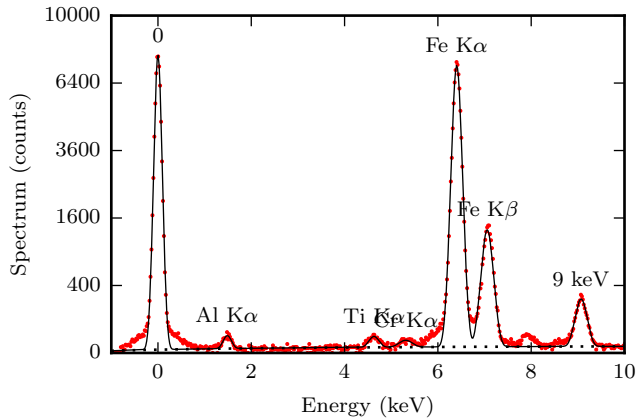


Fig. 7. Red dots show, on a square root y scale, the spectrum of the photons entering through both apertures up to 10 keV. This plot reveals three more discrete energies (between 0 and Fe  $K\alpha$ ) in addition to the three expected ones. Black line depicts the least squares fit using 7 Gaussian peaks and a second degree polynomial background (dotted line). This allows us to identify the three small peaks (as Al  $K\alpha$ , Ti  $K\alpha$ , and Cr  $K\alpha$ ), to conclude that the nominal 9 keV beam is actually closer to 9.1 keV, and also to measure the relative intensities of the 6 lines. The small peak at  $\sim 8$  keV is not a new peak, but the convolution of the Al  $K\alpha$  and Fe  $K\alpha$  peaks. While also  $K\beta$  peaks of Al, Ti and Cr must be present, their contribution can be neglected.

not have a constant intensity (thus the Poisson process is not an accurate description), resulting in higher measured spectra than the fit in both 1 and 5 photons areas.

For the 3 most intense lines (Fe  $K\alpha$ , Fe  $K\beta$ , and  $\sim 9$  keV) we indexed the peaks with corresponding 3 digit labels, showing that for the vast majority of pile-up events (i.e., combinations

of photons), the exact number of photons from each of the 6 fundamental lines can be accurately extracted from the pile-up signal.

The line widths resulting from this fit are larger than the expected SDD performance (e.g., at Mn  $K\alpha$  5.89 keV, the expected line width is 120 eV FWHM and we obtained 222 keV). However, the most likely source of extra noise is already identified in subsection II-B, and could be reduced with hardware improvements. The approach presented here already allows us to recover timing, pile-up and clipping information.

#### IV. EPIXS PIXEL DETECTORS: SDD SUCCESSORS

ePixS [11], [12] is a 2D hybrid pixel detector with an array of  $10 \times 10$   $500 \mu\text{m} \times 500 \mu\text{m}$  pixels, where each pixel has a spectroscopic performance (noise  $\sigma$  of  $8e^-$  or  $\sim 30$  eV, and measured line width of  $\sim 215$  eV FWHM at Mn  $K\alpha$ ) approaching that of SDDs. The ePixS energy resolution is very similar to that in subsection III-F, thus the spectral pile-up decomposition presented in this paper is equally applicable to ePixS detectors.

Fig. 9 shows an  $^{55}\text{Fe}$  source spectrum measured with an ePixS detector, yielding Mn fluorescence: Mn  $K\alpha$  at 5.90 keV and Mn  $K\beta$  at 6.49 keV (reproduced with permission from [10]). The same spectrum is (a) integrated over all pixels and (b) shown separated in individual pixels.

The ePixS camera is built on the ePix platform [13], providing a large number of spectroscopic imaging pixels in a compact, robust and affordable camera package [10].

#### V. CONCLUSION

In standard spectroscopy applications there is often a complex spectrum with a multitude of peaks which need to be resolved and matched to a specific element.

In contrast, at an x-ray FEL there are often only a few photon energies involved in an experiment. Such a situation greatly simplifies the measurement. SDDs can bring significant contributions at FELs in (1) photon counting, (2) spectrum measurements, and (3) background measurements and set-up optimization.

Often only a few photon energies are present, allowing measurement of 0 to 5 photons with (1) spectral pile-up deconvolution, (2) accurate spectroscopic photon counting, and (3) virtual multichannel (position sensitive) measurements, by using peak timing (radius) information.

The analytic approach presented here permits accurate decomposition of individual photon energies and interaction radii from pile-up events of 0 to 5 photons sampled from 6 monochromatic lines and two areas of one single SDD. This is useful not only for SDDs but for any applications of pile-up deconvolution and time/position extraction, like spectroscopy with transition edge sensors [14] or low-noise spectroscopic imaging with integrating pixel detectors [15].

The usefulness of silicon drift detectors will continue into the x-ray FEL era of science. Their successors, the ePixS spectroscopic, hybrid pixel detectors already offer hundreds of pixels with similar performance in a compact, robust and affordable package, particularly useful in x-ray FELs [16].

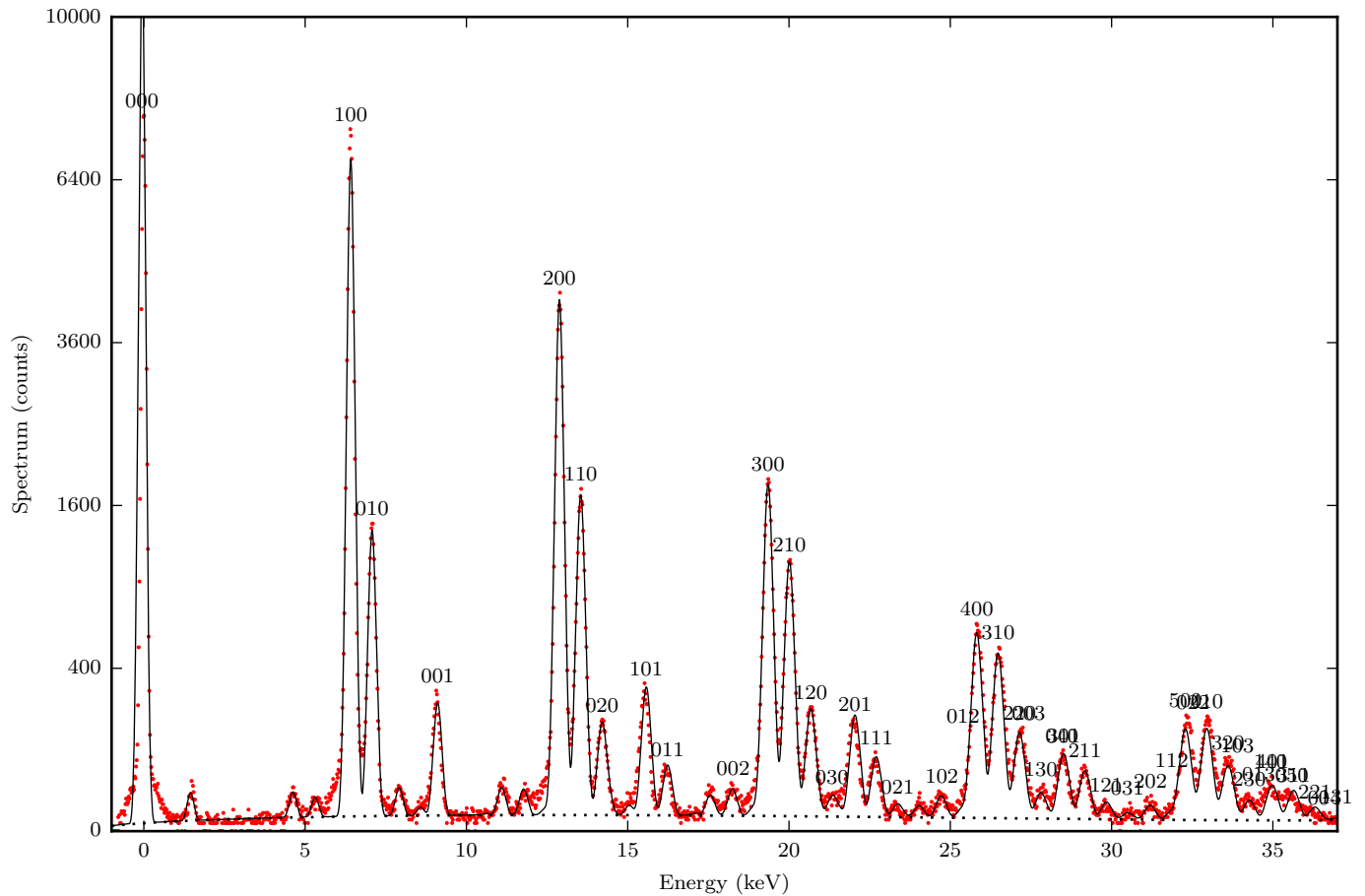


Fig. 8. Red dots show (on a square root y scale) the spectrum of photons entering through both apertures. Black line depicts the least squares fit using a fitting model using the theoretical peak positions of the 7 fundamental lines (Al  $K\alpha$ , Ti  $K\alpha$ , Cr  $K\alpha$ , Fe  $K\alpha$ , Fe  $K\beta$ , and  $\sim 9$  keV) and their relative intensities (as determined in Fig. 7), accurate models for pile-up and peak width as functions of energy, a second-degree polynomial for the background (dotted line), and a Poisson process model. The fit is remarkably successful in fitting the plethora of peaks, using only the fundamental peaks and mathematical modeling. The FEL beam does not have a constant intensity (thus the Poisson process is not an accurate description), resulting in higher peaks than the fit in both 1 and 5 photons areas. For the 3 most intense lines (Fe  $K\alpha$ , Fe  $K\beta$ , and  $\sim 9$  keV) we indexed the peaks with corresponding 3 digit labels (representing the number of photons from each of the 3 lines), showing that for the vast majority of pile-up events (i.e., combinations of photons), the exact number of photons from each of the 6 fundamental lines can be accurately extracted from the pile-up signal.

#### GLOSSARY

CSPAD:	Cornell-SLAC Pixel Array Detector
CXI:	Coherent X-ray Imaging instrument at LCLS
ePix:	SLAC hybrid pixel detector platform
ePixS:	Spectroscopic pixel detector in the ePix family
FEL:	Free-Electron Laser
FWHM:	Full Width at Half Maximum ( $\sim 2.355 \sigma$ )
LCLS:	Linac Coherent Light Source at SLAC
SDD:	Silicon Drift Detector
SLAC:	SLAC National Accelerator Laboratory
XPP:	X-ray Pump-Probe instrument at LCLS

#### ACKNOWLEDGMENT

Use of the Linac Coherent Light Source (LCLS), SLAC National Accelerator Laboratory, is supported by the U.S.

Department of Energy, Office of Science, Office of Basic Energy Sciences under Contract No. DE-AC02-76SF00515.

#### REFERENCES

- [1] E. Gatti and P. Rehak, "Semiconductor drift chamber — an application of a novel charge transport scheme," *Nuclear Instruments and Methods in Physics Research*, vol. 225, no. 3, pp. 608 – 614, 1984. [Online]. Available: [https://dx.doi.org/10.1016/0167-5087\(84\)90113-3](https://dx.doi.org/10.1016/0167-5087(84)90113-3)
- [2] P. Emma, R. Akre, J. Arthur, R. Bionta, C. Bostedt, J. Bozek, A. Brachmann, P. Bucksbaum, R. Coffee, F.-J. Decker *et al.*, "First lasing and operation of an ångström-wavelength free-electron laser," *Nature Photonics*, vol. 4, no. 9, pp. 641–647, 2010. [Online]. Available: <https://dx.doi.org/10.1038/nphoton.2010.176>
- [3] G. Blaj, P. Caragiulo, G. Carini, S. Carron, A. Dragone, D. Freytag, G. Haller, P. A. Hart, R. Herbst, S. Herrmann, J. Hasi, C. Kenney, B. Markovic, K. Nishimura, S. Osier, J. Pines, J. Segal, A. Tomada, and M. Weaver, "Detector development for the Linac Coherent Light

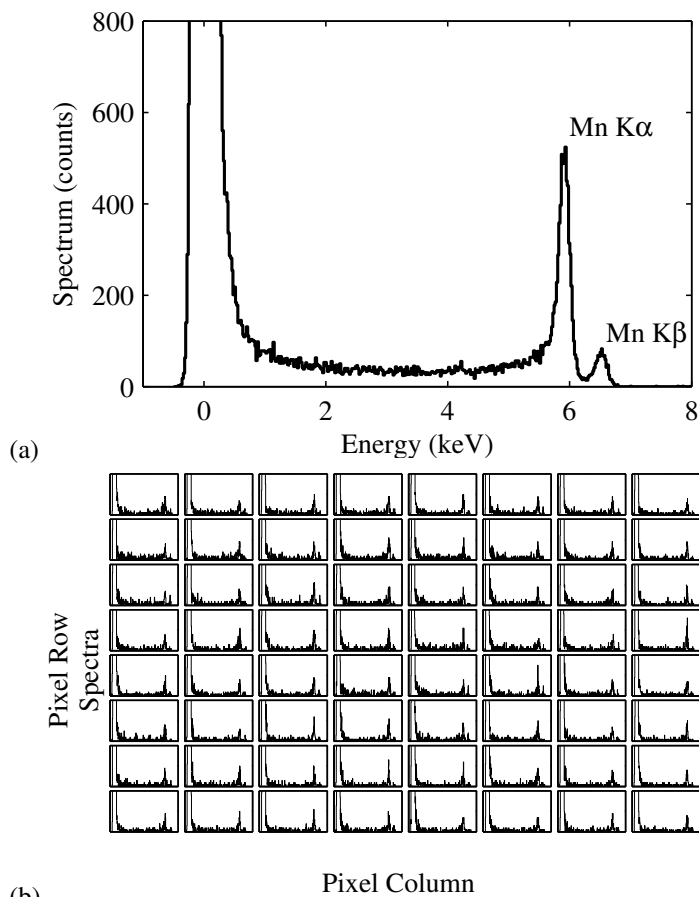


Fig. 9. The ePixS spectroscopic, hybrid pixel detector (reproduced with permission from [10]): (a) ePixS spectrum obtained over all pixels using an  $^{55}\text{Fe}$  source, generating characteristic Mn K $\alpha$  (5.9 keV) and Mn K $\beta$  (6.5 keV) photons, showing the low noise operation with a resulting line width of 225 keV at Mn K $\alpha$ . (b) Shows the same data collected in individual pixels in an  $8 \times 8$  pixel array.

- Source," *Synchrotron Radiation News*, vol. 27, no. 4, pp. 14–19, 2014. [Online]. Available: <https://dx.doi.org/10.1080/08940886.2014.930803>
- [4] W. Guo, R. P. Gardner, and C. W. Mayo, "A study of the real-time deconvolution of digitized waveforms with pulse pile up for digital radiation spectroscopy," *Nuclear Instruments and Methods in Physics Research Section A: Accelerators, Spectrometers, Detectors and Associated Equipment*, vol. 544, no. 3, pp. 668 – 678, 2005. [Online]. Available: <https://dx.doi.org/10.1016/j.nima.2004.12.036>
- [5] M. Chollet, R. Alonso-Mori, M. Cammarata, D. Damiani, J. Defever, J. T. Delor, Y. Feng, J. M. Glowina, J. B. Langton, S. Nelson, K. Ramsey, A. Robert, M. Sikorski, S. Song, D. Stefanescu, V. Srinivasan, D. Zhu, H. T. Lemke, and D. M. Fritz, "The X-ray Pump-Probe instrument at the Linac Coherent Light Source," *Journal of Synchrotron Radiation*, vol. 22, no. 3, pp. 503–507, May 2015. [Online]. Available: <https://doi.org/10.1107/S1600577515005135>
- [6] S. Boutet and G. Williams, "The Coherent X-ray Imaging (CXI) instrument at the Linac Coherent Light Source (LCLS)," *New Journal of Physics*, vol. 12, no. 3, p. 035024, 2010. [Online]. Available: <https://dx.doi.org/10.1088/1367-2630/12/3/035024>
- [7] G. Blaj, P. Caragiulo, G. Carini, S. Carron, A. Dragone, D. Freytag, G. Haller, P. Hart, J. Hasi, R. Herbst, S. Herrmann, C. Kenney, B. Markovic, K. Nishimura, S. Osier, J. Pines, B. Reese, J. Segal, A. Tomada, and M. Weaver, "X-ray detectors at the Linac Coherent Light Source," *Journal of Synchrotron Radiation*, vol. 22, no. 3, pp. 577–583, 2015. [Online]. Available: <https://dx.doi.org/10.1107/S1600577515005317>
- [8] R. Redus, *Digital Pulse Processors, Theory of Operation*, Amptek Inc, 2009. [Online]. Available: <https://amptek.com/pdf/dpp%5Ftheory.pdf>
- [9] E. Gatti, M. Sampietro, and P. Manfredi, "Optimum filters for detector charge measurements in presence of 1/f noise," *Nuclear Instruments and Methods in Physics Research Section A: Accelerators, Spectrometers, Detectors and Associated Equipment*, vol. 287, no. 3, pp. 513 – 520, 1990. [Online]. Available: [https://dx.doi.org/10.1016/0168-9002\(90\)91571-R](https://dx.doi.org/10.1016/0168-9002(90)91571-R)
- [10] K. Nishimura, G. Blaj, P. Caragiulo, G. Carini, A. Dragone, G. Haller, P. Hart, J. Hasi, R. Herbst, S. Herrmann, C. Kenney, M. Kwiatkowski, B. Markovic, S. Osier, J. Pines, B. Reese, J. Segal, A. Tomada, and M. Weaver, "Design and performance of the ePix camera system," *AIP Conference Proceedings*, vol. 1741, no. 1, p. 040047, 2016. [Online]. Available: <https://dx.doi.org/10.1063/1.4952919>
- [11] J. Hasi, G. Blaj, P. Caragiulo, A. Dragone, G. Haller, P. Hart, R. Herbst, C. Kenney, B. Markovic, K. Nishimura, S. Osier, J. Pines, J. Segal, and A. Tomada, "High channel count x-ray spectroscopy detector for x-ray FELs," talk presented at the Synchrotron Radiation Instrumentation 2015 Conference, New York, NY, Jun 2015.
- [12] A. Dragone, P. Caragiulo, B. Markovic, G. Blaj, J. Hasi, J. Segal, A. Tomada, K. Nishimura, R. Herbst, P. Hart, S. Osier, J. Pines, C. Kenney, and G. Haller, "ePixS: a high channel count x-ray spectroscopy detector for x-ray FELs," 2015, talk presented at the IEEE Nuclear Science Symposium and Medical Imaging Conference (NSS/MIC), San Diego, CA, Nov 2015.
- [13] A. Dragone, P. Caragiulo, B. Markovic, R. Herbst, K. Nishimura, B. Reese, S. Herrmann, P. A. Hart, G. Blaj, J. Segal, A. Tomada, J. Hasi, G. Carini, C. Kenney, and G. Haller, "ePix: a class of front-end ASICs for second generation LCLS integrating hybrid pixel detectors," in *2013 IEEE Nuclear Science Symposium and Medical Imaging Conference (2013 NSS/MIC)*. IEEE, Oct 2013, pp. 1–5. [Online]. Available: <https://dx.doi.org/10.1109/NSSMIC.2013.6829505>
- [14] K. Irwin and G. Hilton, *Transition-Edge Sensors*. Berlin, Heidelberg: Springer, 2005, ch. 3, pp. 63–150. [Online]. Available: <https://dx.doi.org/10.1007/10933596%5F3>
- [15] G. Blaj, P. Caragiulo, A. Dragone, G. Haller, J. Hasi, C. J. Kenney, M. Kwiatkowski, B. Markovic, J. Segal, and A. Tomada, "X-ray imaging with ePix100a, a high-speed, high-resolution, low-noise camera," in *SPIE Proceedings*, vol. 9968. International Society for Optics and Photonics, 2016, pp. 99 680J–99 680J–10. [Online]. Available: <https://dx.doi.org/10.1117/12.2238136>
- [16] G. Blaj, P. Caragiulo, G. Carini, A. Dragone, G. Haller, P. Hart, J. Hasi, R. Herbst, C. Kenney, B. Markovic, K. Nishimura, J. Pines, J. Segal, C. Tamma, and A. Tomada, "Future of ePix detectors for high repetition rate FELs," *AIP Conference Proceedings*, vol. 1741, no. 1, p. 040012, 2016. [Online]. Available: <https://dx.doi.org/10.1063/1.4952884>